



Hydrothermal synthesis and characterization of CuO–CoO/TiO₂ for photocatalytic degradation of methylene blue under visible light and catalytic reduction of P-nitrophenol

Z. Moradi Shammi¹ · A. H. Kianfar¹ · M. M. Momeni¹

Received: 21 January 2020 / Accepted: 18 July 2020 / Published online: 27 July 2020
© Springer Science+Business Media, LLC, part of Springer Nature 2020

Abstract

CuO–CoO/TiO₂ has been prepared using TiO₂-P-25, Cu(acac)₂/Co(acac)₃ (sample 1) and Cu(NO₃)₂/Co(NO₃)₂ (sample 2) by hydrothermal method. DRS, CV, EDX, XRD, XPS, Raman, FE-SEM, and TEM have been used for structural, optical, and morphological analyses of the samples. The anatase phase formation of the samples has been identified by powder X-ray diffraction and Raman spectroscopy. Cu and Co metals were present as CuO and CoO in both samples, according to XPS and Raman spectroscopy data. UV–Vis–NIR reflectance and cyclic voltammetry analysis were used to determine the absorption nature of the samples. Through these techniques, the band gap values of samples 1 and 2 were determined as 2.0 and 2.5 eV, respectively. Nanotube/nanosheet and nanoparticle morphologies were shown by samples 1 and 2, respectively, based on transmission electron microscopy (TEM) results. The synthesized nanomaterials were applied in the degradation of methylene blue (MB) under visible light. The photocatalytic activity of the samples was studied in the presence and absence of H₂O₂. Degradation time was 4–40 min in the presence of 2 mg of the catalyst. In addition, the samples were used as catalysts in the reduction of P-nitrophenol (PNP) by NaBH₄. UV–Vis spectroscopy was used to monitor the progress of the catalytic and photocatalytic degradation reactions. Furthermore, the catalyst samples were removed and recycled several times. The photocatalytic degradation reaction was carried out in the presence of various free radical scavengers and hydroxyl radical and hole were determined as the main active species for samples 1 and 2, respectively.

1 Introduction

Environmental pollution is a global phenomenon due to its adverse effects on the health of humans, plants, and animals. Industrialization and urbanization are greatly associated with pollution issues. Many organic and industrial effluents have been introduced into the environment to increase water and land pollution problems [1, 2]. Dyes and nitroaromatic compounds are a main group of environmental pollutants. Among nitroaromatic compounds, nitrophenols are widely produced by dyes, pesticides, and pharmaceuticals from industrial and agricultural activities. Among many

nitrocompounds, P-nitrophenol (PNP), which is used in the treatment of eye and skin irritation, is capable of causing cyanosis, confusion, and unconsciousness [3–5]. There are several methods for the reduction of P-nitrophenol (PNP) to p-aminophenol (PAP) such as catalytic hydrogenation, electrolytic reduction, metal/acid reduction, and chemical reduction. In addition to being economically viable, some of these methods create many problems during the reduction of PNP to PAP [6]. Chemical reduction of PNP is a relatively green method in which NaBH₄ is used to reduce PNP to PAP as a starting material for the preparation of antioxidants, analgesics, febrifuge drugs, and dyes. The disadvantage of this method is the long reaction time [7, 8]. The application of an appropriate catalyst to reduce the reaction time is a challenge for researchers [9, 10]. Dyes are environmental contaminants generally produced from such sources as textile, paper, and plastic industries. These compounds prevent sunlight permeation into the water, decrease the photosynthetic action, and cause death of aquatics. In addition, most dyes contain known carcinogenic aromatic groups. Among these chemical compounds, methylene blue

Electronic supplementary material The online version of this article (<https://doi.org/10.1007/s10854-020-04044-9>) contains supplementary material, which is available to authorized users.

✉ A. H. Kianfar
akianfar@cc.iut.ac.ir

¹ Department of Chemistry, Isfahan University of Technology, Isfahan 84156/83111, Iran

(MB) is a heterocyclic dye with toxic and harmful effects on water [11, 12]. Photocatalytic methods have been introduced as green and low-cost approaches for the effective elimination of dyes from wastewaters under mild conditions [13]. Given its large surface area, structure, fast electron transport, and low-charge recombination, titanium dioxide (n-type semiconductor) has shown enhanced performance in photocatalytic and catalytic reactions [14]. Regrettably, UV light irradiation can generate electron–hole pairs due to the high band gap of titanium dioxide ($E_g = 3.0\text{--}3.2$ eV) [15, 16]. In addition, electron–hole pairs on the surface recombine very fast, resulting in low photocatalytic and catalytic efficiency [17]. To overcome these obstacles, different methods have been developed to enhance the photocatalytic and catalytic efficiency of TiO_2 . Loading of noble metals over titanium dioxide has been reported as an effective method to restrain the electron–hole recombination. Therefore, noble metals such as Pt, Au, Pd, and Ag have been extensively used in TiO_2 to improve the electron–hole separation and expand the absorption of UV light active TiO_2 semiconductor to the visible light region [18–21]. Nevertheless, the photocatalytic and catalytic performance of TiO_2 can be further improved by the use of bimetallic compounds (BM) [22]. A combination of the properties associated with two individual metals is expected to be shown by BM deposited on TiO_2 . Copper oxide, a p-type semiconductor, is considered as a supporting material mixed with n-type photocatalysts such as TiO_2 [23, 24]. Cobalt oxide, a p-type appropriate semiconductor, is also applied in mixtures such as CuO , WO_3 [25, 26]. Thus, metal oxides (p-type semiconductors) supported on titanium dioxide (n-type semiconductor) improve the absorption of visible light by titanium dioxide. There are different techniques to dope metals on the nano titanium dioxide surface such as sol–gel, hydrothermal, solvothermal, and microwave-assisted methods [9]. The hydrothermal method has shown to be promising with respect to the enhancement of catalytic and photocatalytic activities in the elimination of organic pollutants from waste water. Process parameters such as concentration of alkaline solution, structure of raw materials, reaction temperature, reaction time, and the effect of acid on washing affect the morphology of the titanium dioxide obtained from hydrothermal methods [27].

In our research group, many efforts have been made to expand the absorption of titanium dioxide to visible light using various compounds through reducing the band gap. In these studies, titanium dioxide was supported on some metal oxides such as CuO , NiO , and V_2O_5 prepared from metal shift base complexes [28–30]. In continuation of our studies on the photocatalytic properties of mixed oxides, the effect of metal salts and complexes on TiO_2 morphology and its catalytic and photocatalytic activities have been studied. Cobalt(III) acetylacetonate/copper(II) acetylacetonate (sample 1) and cobalt(II) nitrate/copper(II) nitrate (sample

2) were applied as copper and cobalt oxide sources, respectively. XRD, XPS, Raman, SEM, TEM, DR–UV–Vis, CV, and N_2 adsorption–desorption analyses were then used to characterize $\text{CuO}\text{--}\text{CoO}/\text{TiO}_2$. Methylene blue and P-nitrophenol were used as pollutants to study the photocatalytic and catalytic activities of the samples under visible light.

2 Experimental

2.1 Materials

All chemicals including sodium hydroxide, $\text{Cu}(\text{acac})_2$, $\text{Co}(\text{acac})_3$, $\text{Cu}(\text{NO}_3)_2$, $\text{Co}(\text{NO}_3)_2$, and methylene blue were obtained from Sigma Aldrich Chemical Co. NaBH_4 , para, and amino nitrophenol were supplied by Merck Chemical Co. TiO_2 nanoparticles (P-25) were purchased from Hanau-Wolfgang Co. (Germany).

2.2 Characterizations

UV–Visible spectra were recorded on a JASCO V-750 spectrophotometer. Transmission electron microscopy (TEM) was carried out using a Philips (model EM 208S, 100 kV, W Filament) instrument. Cu and Co contents of the catalysts were measured using inductively coupled plasma optical emission spectrometry (ICP-OES, Perkin Elmer, Optima 7300DV). X-ray diffraction (XRD) patterns were recorded using a Scintag X-ray diffractometer with X-ray wavelength of 1.54 Å ($\text{CuK}\alpha$ radiation source). A Physical Electronics PHI5700 photoelectron spectrometer with $\text{AlK}\alpha$ (1486.6 eV) radiation source was used to conduct X-ray photoelectron spectrometry (XPS). Raman spectroscopy was performed on a Takvm P50COR10 apparatus using a green laser (530 nm). A JEOL JSM-6390A scanning electron microscope (SEM) equipped with an energy dispersive X-ray detector was used to perform morphological observations. A Shimadzu 2450 instrument was used to perform ultraviolet–visible diffuse reflectance spectroscopy (UV–Vis DRS). Kubelka–Munk equation was used to calculate the band gap energy of the samples. N_2 adsorption–desorption (BET) was used to evaluate the pore structure, size, and kind of isotherms of the two samples.

2.3 Preparation of samples 1 and 2

Samples of different surface areas were prepared using hydrothermal method with different metal salts nitrates and acetyl acetonates. Throughout the experiments, the NaOH concentration was set at 10 M and the hydrothermal reaction was carried out at constant temperature of 180 °C for 24 h to obtain samples 1 and 2 with different effective surface areas. First, 1.00 g of TiO_2 nanoparticles (P-25)

was dispersed in 50 mL of 10 M NaOH aqueous solution using a magnetic stirrer at 50 °C for 30 min, followed by the addition of the metal salts (0.261 g of $\text{Cu}(\text{acac})_2$ and 0.356 g of $\text{Co}(\text{acac})_3$ for sample 1 and 0.261 g of $\text{Cu}(\text{NO}_3)_2$ and 0.356 g of $\text{Co}(\text{NO}_3)_2$ for sample 2) to the suspension. Having been stirred for 1 h, the mixture was transferred into a 50 mL Teflon-lined stainless steel autoclave and subjected to hydrothermal treatment at 180 °C for 24 h. Afterwards, the contents of the autoclave were allowed to cool down to room temperature. The product formed was treated with 50 mL of 0.1 M HCl overnight, followed by washing with distilled water until the pH of the water reached 7. The sample was then filtered, dried at 80 °C, spread into a ceramic boat, and calcined in air at 350 °C for 5 h at a rate of 2 °C/min. The products obtained were denoted as samples 1 and 2 [31–33].

2.4 Photocatalytic activity

2.4.1 Photodegradation of MB by samples 1 and 2

2 mg of sample 1 or 2 was used in the degradation of 5 mL of an aqueous solution of MB (10 ppm) in the absence and presence of 1 mL of H_2O_2 (0.1 M) under visible light irradiation. UV–Vis spectroscopy was used to monitor the progress of the reaction. All the photocatalytic experiments were performed at ambient temperature. The reaction times for degradation of MB were determined as 7 and 4 min in the absence and presence of 1 mL of H_2O_2 (0.1 M) for sample 1, respectively. In addition, for sample 2, the reaction times were 40 and 10 min in the absence and presence of 1 mL of H_2O_2 (0.1 M), respectively. The absorption spectra of MB were recorded for 1 and 5 min for samples 1 and 2, respectively.

2.4.2 Free radical scavenger tests

The photocatalytic degradation of MB is affected by the various free radical scavengers. Therefore, the reaction was studied using some radical scavengers to determine the active species. In order to investigate the effect of hydroxyl radicals ($\cdot\text{OH}$), superoxide radicals ($\cdot\text{O}_2^-$), and holes (h^+), p-benzoquinone (BQ), ethylenediaminetetraacetic acid (EDTA), and isopropyl alcohol (IPA) scavengers were used, respectively. In this study, the effect of the cited scavengers on both samples was evaluated. For every sample, a solution was prepared using 1 mmol of the scavenger, 2 mg of the catalyst, 5 mL of an aqueous solution of MB (10 ppm), and 1 mL of H_2O_2 (0.1 M) under visible light irradiation at room temperature.

2.5 Catalyst activity

2.5.1 Reduction of PNP to PAP by samples 1 and 2

1.5 mL of an aqueous solution of 10^{-4} M PNP and 0.5 mL of fresh 10^{-2} M NaBH_4 were added into a quartz cell. 2 mg of sample 1 or 2 was then added to the mixture to start the reduction reaction. UV–Vis spectroscopy was used to follow the progress of the reaction. 4-NP has a maximum absorption peak at 318 nm, which changes to 400 nm upon the addition of NaBH_4 due to the formation of phenolate. After PNP reduction, the peak at about 400 nm is flattened and an amine peak appears at 300 nm. The concentration chart was plotted vs. absorption to evaluate the reaction rate.

3 Results and discussion

3.1 Structure characterization

3.1.1 FE-SEM and EDX

FE-SEM spectroscopy was carried out to study the morphology of sample surfaces. Under the same conditions, two different reactants (metal salts) were applied to prepare samples 1 and 2 nanocompounds. Based on the FE-SEM images, two different shapes were obtained for these nanocompounds. The FE-SEM image of sample 1 is shown in Fig. S1a, b. According to the micrograph, sample 1 has a nanosheet structure. In addition, the FE-SEM image of sample 2 is shown in Fig. S1b. A sponge-like structure was obtained for this compound. On the other hand, the average particle size of this sample was found to be 20 nm [34–36].

Figure S2a, b shows the EDX spectra of samples 1 and 2, respectively. The spectra confirm the presence of Co, Cu, Ti, and O in both samples. The formation of the samples is clearly confirmed by the EDX spectra.

3.1.2 TEM studies

The TEM micrographs of samples 1 and 2 are shown in Fig. 1a, b, respectively. In sample 1, the presence of the holes inside the fibrous like structures confirms the formation of nanotubes and nanosheets. The inner and outer diameters of the nanotubes were found to be 5 and 13 nm, respectively. Furthermore, the diameter of nanosheets was found to be 43 nm (Fig. 1a). According to the TEM image of sample 2 (Fig. 1b), the nanoparticles are spherically shaped [37, 38].

Hydrothermal method has been used to dope mixed oxides on TiO_2 surface in this work. Surface morphology is reportedly influenced by different conditions such as temperature, heating time, NaOH concentration, and acid washing step. In this study, two samples were prepared

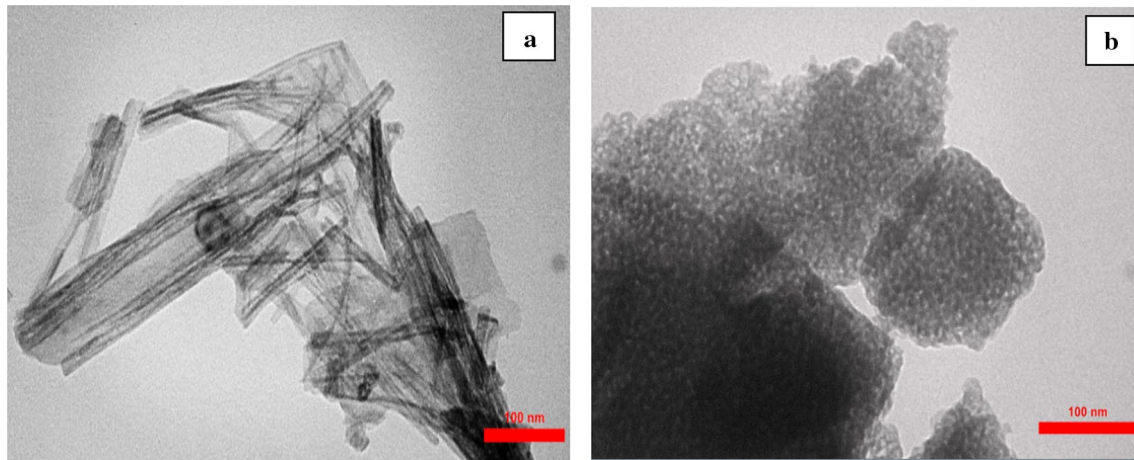


Fig. 1 TEM image of **a** sample 1, **b** sample 2

under identical conditions using different metal salts. According to FE-SEM and TEM, sample 1 which contains $\text{Cu}(\text{acac})_2$ and $\text{Co}(\text{acac})_3$ is of nanotube and nanosheet morphology. However, sample 2 which contains $\text{Cu}(\text{NO}_3)_2$ and $\text{Co}(\text{NO}_3)_2$ is a nanoparticle. In addition to the conditions pointed out, the type of metal salt seems to affect the surface morphology in hydrothermal method [27, 34–37].

3.1.3 X-ray diffraction

In order to determine the crystal planes and obtain some information on the structure of nanocomposites, the X-ray diffraction (XRD) was carried out. Fig. S3 shows the XRD patterns of samples 1 and 2, prepared at 350 °C. The Bragg reflections of sample 1 were observed at angles of 25.325° (101), 38.601° (112), 48.074° (200), 55.106° (211), 62.750° (204), 68.842° (116), and 75.129° (215). However, for sample 2, the corresponding angles were 25.307° (101), 38.570° (112), 48.043° (200), 55.068° (105), 62.689° (204), 68.750° (116), and 75.050° (215). Based on these reflections, anatase phase was confirmed for TiO_2 in both samples (JCPDS files No. 01-0562 and 83-2243 for samples 1 and 2, respectively) [37, 38]. The presence of CuO is confirmed in both samples by peaks at 35.610° (110), 38.686° ($\bar{1}11$), and 48.659° ($\bar{2}02$) for sample 1 and 35.744° ($\bar{1}11$), 38.958° (111), 50.850° ($\bar{2}02$), and 66.229° (022) for sample 2 (JCPDS files no. 80-1916 and 01-1117 for samples 1 and 2, respectively) [37, 38]. Furthermore, the composition of CoO is identified by the plane at 34.477° (111), 40.450° (200), and 57.220° (220) for sample 1 and 35.500° (111), and 58.350° (220) for sample 2 (JCPDS files no. 75-0419 and 42-1300 for samples 1 and 2, respectively) [39, 40].

3.1.4 X-ray photoelectron spectroscopy

The XPS spectrum of sample 1 is shown in Fig. 2. As observed in Fig. 2b, the high-resolution $\text{Ti}2p$ XPS spectra of sample 1 and the peaks at 458.90 and 464.50 eV are associated with ($\text{Ti}2p_{3/2}$) and ($\text{Ti}2p_{1/2}$), respectively. The high-resolution $\text{O}1s$ XPS spectrum of sample 1 is shown in Fig. 2c. The peak at 531.3 eV is attributed to the hydroxyl oxygen. The XPS spectrum of CoO is shown in Fig. 2d. The reported value of Co(II) in CoO is 780 eV along with the presence of its characteristic shakeup satellite peak at 786.3 eV. The peak positions measured for this sample are 781.10 and 787.60 eV, confirming the presence of CoO and divalent cobalt as CoO . Moreover, Fig. 2e shows the XPS spectrum of CuO . The main peaks of Cu(II) at 932.70 eV ($\text{Cu} 2p_{3/2}$) and 952.00 eV ($\text{Cu} 2p_{1/2}$) and the characteristic shakeup satellite peaks observed at 941.90 and 960.00 eV, respectively, confirm the presence of CuO in the composition [40–42].

The XPS spectrum of sample 2 is shown in Fig. 3. As observed in Fig. 3b, the high-resolution $\text{Ti}2p$ XPS spectrum of sample 2 shows peaks at 459.50 and 464.50 eV, which are due to ($\text{Ti}2p_{3/2}$) and ($\text{Ti}2p_{1/2}$ of Ti^{4+}), respectively. The high-resolution $\text{O}1s$ XPS spectrum of sample 2 is shown in Fig. 3c. The peak at 530.50 eV corresponds to the hydroxyl oxygen. The high-resolution XPS spectrum of $\text{Cu}2p$ of sample 2 (Fig. 3d) shows four peaks at 932.50, 952.00, 944.00, and 957.00 eV. The peaks at binding energies of 932.50 and 952.00 eV are ascribed to the $\text{Cu}2p_{3/2}$ and $\text{Cu}2p_{1/2}$, respectively. Meanwhile, the peaks at 944.00 and 957.00 eV corresponding to the binding energy shakeup satellites are due to pure CuO . The binding energies of pure CoO are observed at 781.50 and 788.00 eV (Fig. 3e) [40–42].

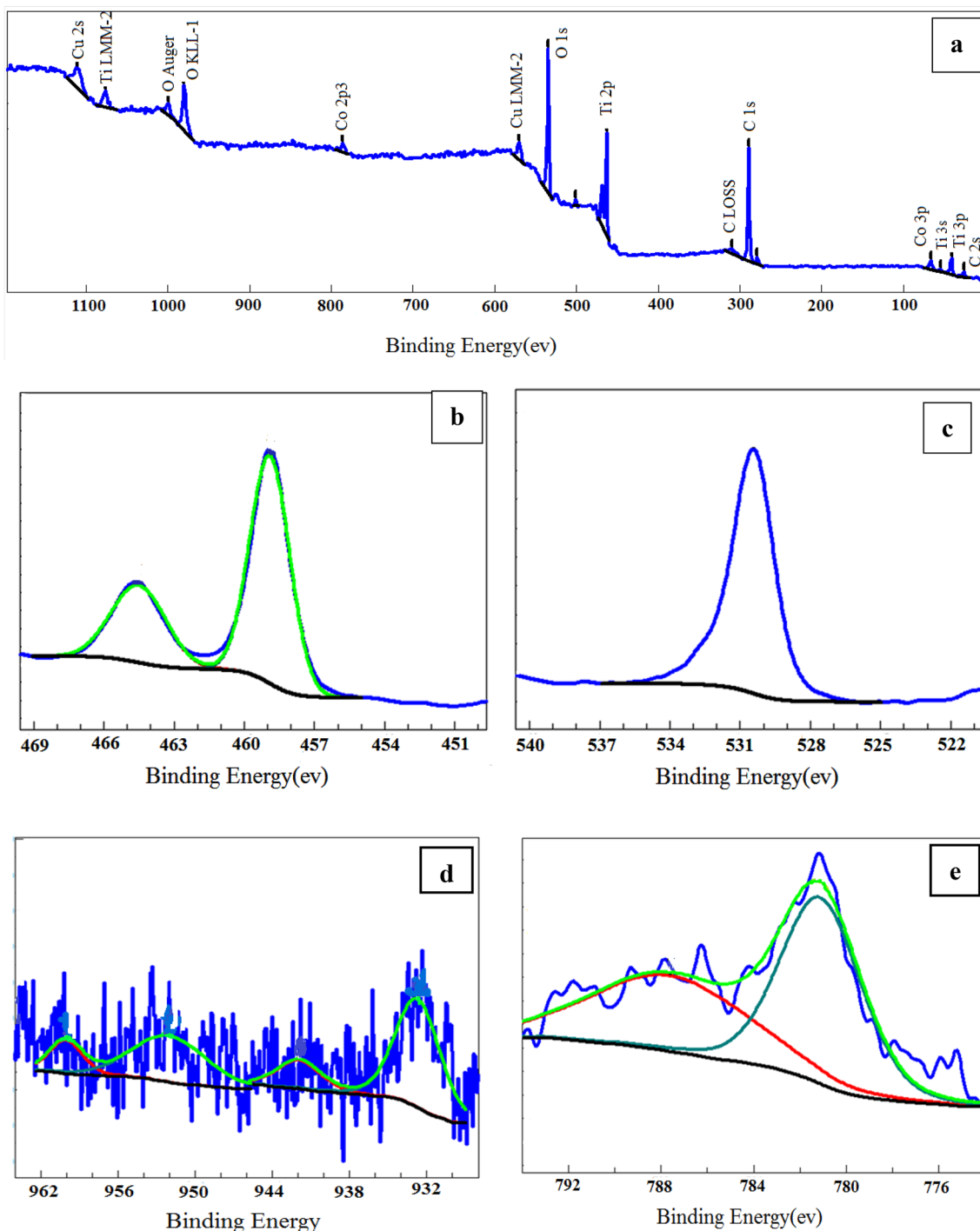


Fig. 2 XPS spectra of sample 1 **a** survey spectrum and high-resolution of **b** Ti2p; **c** O1s; **d** Cu2p; and **e** Co2p

3.1.5 Raman spectroscopy

The Raman spectra of both samples and TiO₂ (P-25) are illustrated in Fig. 4. The bands at 153, 643, 401, and 520 cm⁻¹ are assigned to the E_g (153 and 643 cm⁻¹) and B_{1g} (401 and 520 cm⁻¹) modes of anatase TiO₂ crystals for TiO₂ (P-25). The observed peaks at 156, 631, 395, and

514 cm⁻¹ correspond to the E_g (156 and 631 cm⁻¹) and B_{1g} (395 and 514 cm⁻¹) modes of anatase TiO₂ crystals for sample 1. For sample 2, the peaks at 153, 401, 520, and 631 cm⁻¹ correspond to the E_g (153 and 631 cm⁻¹) and B_{1g} (401 and 520 cm⁻¹) modes of anatase TiO₂ crystals. Compared with the undoped sample, the most intense peak at 153 cm⁻¹ shows the blueshift while the peaks at 401, 520,

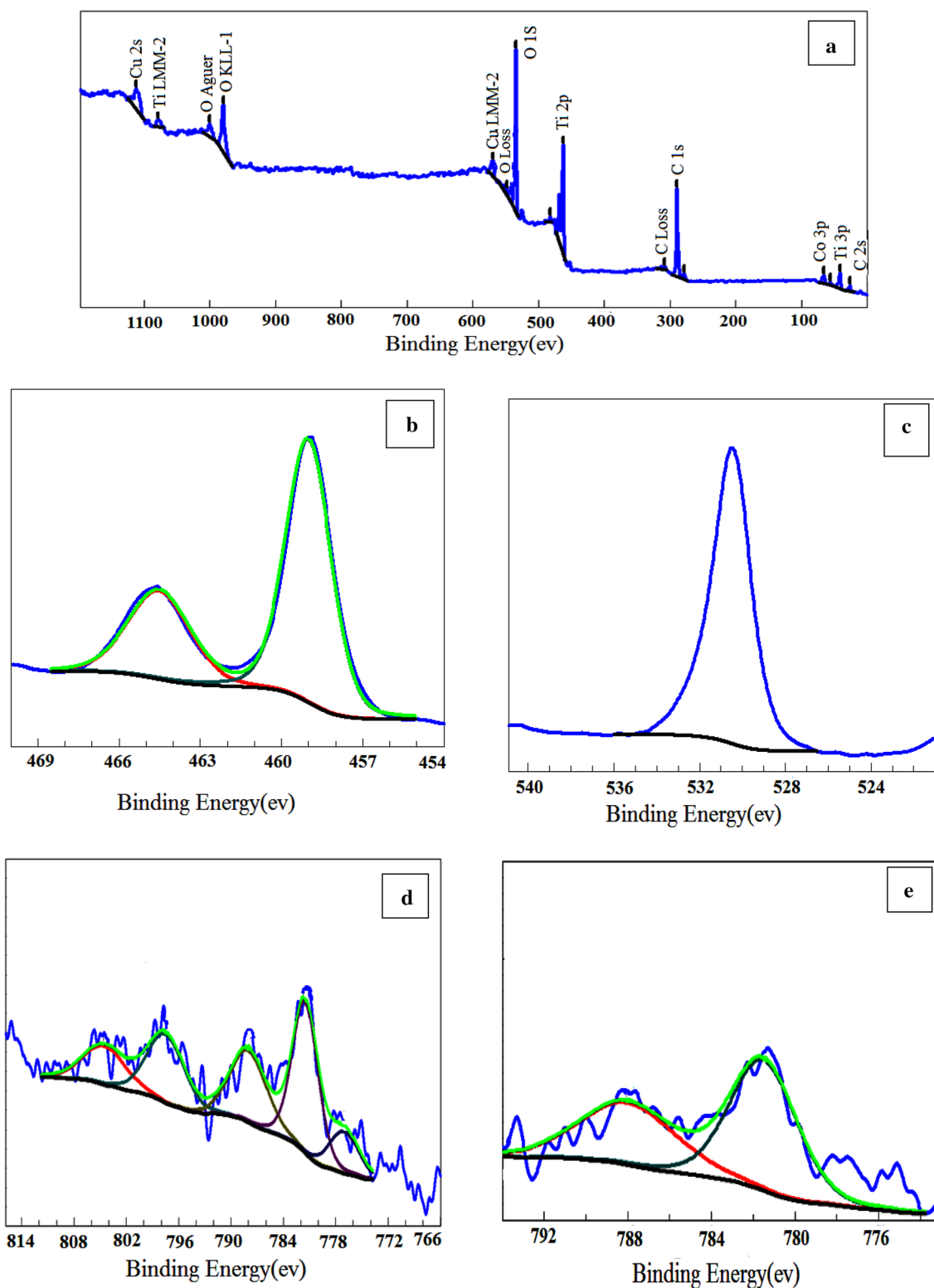


Fig. 3 XPS spectra of sample 2 **a** survey spectrum and high resolution of **b** Ti2p; **c** O1s; **d** Cu2p; and **e** Co2p

and 643 cm^{-1} show redshift in Sample 1. On the other hand, in comparison to bare TiO_2 (P-25), the peak at 643 shows red shift. In addition, the intensity and sharpness of all peaks

are decreased relative to the undoped TiO_2 (P-25). The weak peaks observed at 269 and 695 cm^{-1} are related to the Ag (269 cm^{-1}) and B_{2g} (695 cm^{-1}) modes of CuO for both

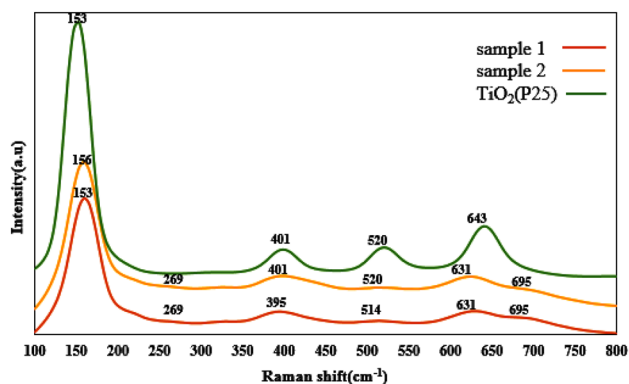


Fig. 4 Raman spectra

samples. The peak at 695 cm^{-1} might be due to A_{1g} mode of CoO , which overlaps with CuO peak for both samples. On the other hand, the peak at 269 cm^{-1} is related to titanate structure of TiO_2 , which overlaps with CuO peak in samples 1 and 2 [43–45]. The results confirmed the formation of CuO-CoO/TiO_2 , which is in agreement with data obtained from the XPS and XRD analyses.

Fig. 5 N_2 adsorption–desorption isotherms of a sample 1; b sample 2

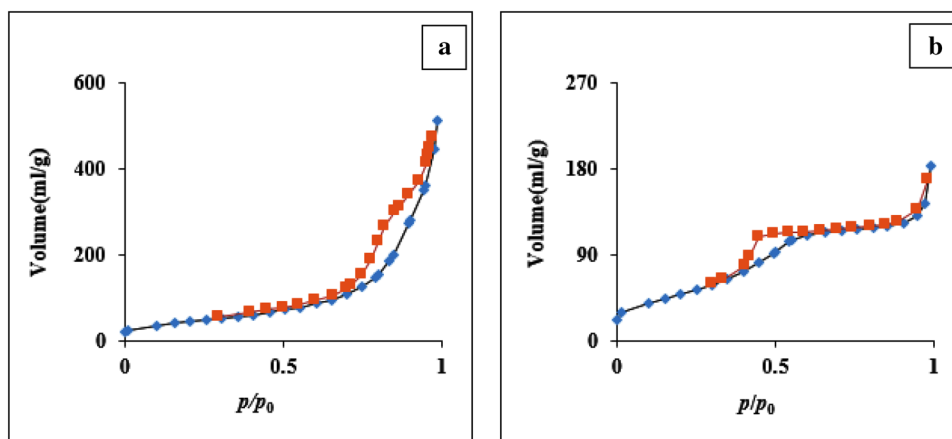
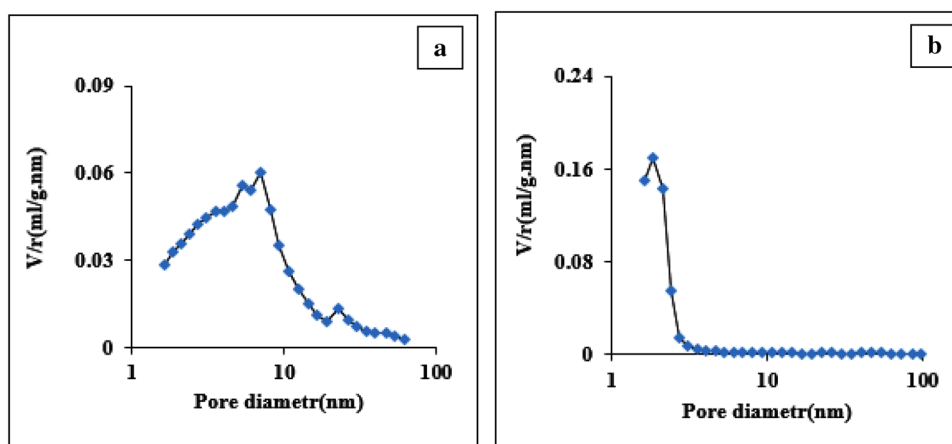


Fig. 6 a Particle size distribution of mesoporous a sample 1; b sample 2



3.2 N_2 adsorption–desorption analysis

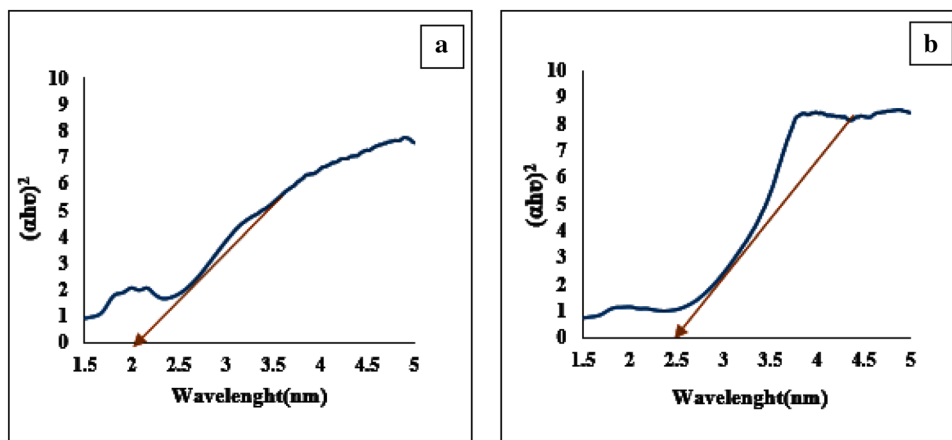
The N_2 adsorption–desorption isotherms of samples 1 and 2 were used to evaluate the pore structure and size. The isotherms of the two samples have classical hysteresis loops, as observed in Fig. 5a, b. The adsorption–desorption isotherms of samples 1 and 2 are classical type IV and V, respectively. A hysteresis loop is known to indicate the presence of mesoporous structure in the samples. The pore size distribution curves of samples 1 and 2 are shown in Fig. 6a, b, respectively. A pore diameter of 6.95 nm and a total pore volume of $0.790\text{ cm}^3\text{ g}^{-1}$ were obtained for sample 1 while the corresponding values for sample 2 were 1.85 nm and $0.282\text{ cm}^3\text{ g}^{-1}$, respectively. Furthermore, BET equation was used to calculate the specific surface areas of the samples. The S_{BET} values were 161.1 and $211.67\text{ m}^2\text{ g}^{-1}$ for samples 1 and 2, respectively. Sample 2 had a smaller pore size and pore volume and a bigger specific surface area compared to sample 1, according to the results. Table 1 shows all the results [42, 46–48].

Table 1 Surface area, pore size, pore volume, and band gap of samples 1, 2, and P25-TiO₂

Sample name	Pore size (nm)	Pore volume (cm ³ g ⁻¹)	S _{BET} (m ² g ⁻¹)	Band gap (eV)
Sample 1	6.95	0.79	161.1	2.0
Sample 2	1.85	0.282	211.67	2.5
TiO ₂ -P25	21.0	50.0	50.0	3.2

3.2.1 UV–Vis Diffuse Reflectance Spectroscopy

Figure S4a, b shows the UV–Vis absorption spectra of the two samples. The samples clearly show a larger photocurrent under visible light irradiation compared with TiO₂ P-25. This causes the easy transfer of the excited electrons in the valance band of the metals to the conduction band of TiO₂. The optical absorbance ($F(R)$) of the samples from Kubelka–Munk formalism (Fig. 7a, b) was used to determine the band gap energy of the photocatalysts. Using this equation, semiconducting materials can be analyzed using a Tauc plot of $[F(R) \cdot hv]^n$ vs. hv where hv is the photon energy and $n = 1/2$ for direct band gap of the photocatalyst. The band gap energies determined for samples 1 and 2 were 2.0 and 2.5, respectively. However, the reported band gap for TiO₂ P-25 is 3.20. According to the results, sample 1 has a smaller band gap than sample 2. Table 1 shows all the band gap values determined [49–51].

Fig. 7 Plot of $[ahv]^2$ vs. photon energy (hv) **a** sample 1; **b** sample 2**Table 2** The HOMO, LUMO levels, and band gap approximated from CV

Compound	E_{OX} vs. Ag/AgCl (V)	HOMO level (eV)	E_{red} vs. Ag/AgCl (V)	LUMO level (eV)	E_g [from CV] (eV)
Sample 1	1.44	- 6.387	- 0.509	- 4.438	1.95
Sample 2	1.86	- 6.807	- 0.586	- 4.361	2.44

3.2.2 Cyclic voltammetry

Slides of 3×1 cm used in cyclic voltammetry were prepared for each sample. The samples were deposited on glass/ITO substrates as a thin layer of nearly 40 nm at slow rates, less than 1 nm/s, by vacuum thermal evaporation. In this experiment, platinum plate and Ag/AgCl couple were applied as auxiliary and reference electrodes, respectively, and the slides containing the thin layer of the sample were used as the working electrode. Cyclic voltammetry tests were carried out at a scan rate of 20 mV/s under nitrogen at room temperature. A solution of 0.1 M tetrabutylammonium phosphorus hexafluoride (TBAPF6) in anhydrous acetonitrile (CH₃CN) was used as the electrolyte [52].

Sample 1 shows a reduction peak at - 0.509 V. The energy level of LUMO was calculated at - 4.438 eV by Eq. 1. In addition, the oxidation peak at 1.44 V, leading to a HOMO level was calculated at - 6.387 eV by Eq. 2. The band gap energy was determined as 1.95 eV, which is in good agreement with the obtained band gap from the optical absorption spectrum (2.0 eV). In sample 2, the reduction and oxidation peaks were observed at - 0.586 and 1.86 V, respectively. The energy levels of LUMO and HOMO were calculated as - 4.361 eV and - 6.807 eV, respectively. Furthermore the band gap energy was determined to be 2.44 eV (the obtained band gap from optical absorption spectrum is 2.5 eV) [22, 53] (Table 2).

$$E_{LUMO} = -e(4.75 + E_{red, vs NHE}) \text{ (eV)} \quad (1)$$

$$E_{HUMO} = -e(4.75 + E_{ox, vs NHE}) \text{ (eV)} \quad (2)$$

$$E_{\text{NHE}} = E_{\text{Ag/AgCl}} + 0.197$$

3.3 Visible light photocatalytic activity of samples 1 and 2

The photocatalytic activity of both samples was determined by monitoring methylene blue degradation in an aqueous solution under visible light irradiation using a Tungsten Lamp (500 W). The intensity of the light was 200 mW/cm². The intensity and calibration of light source were measured by Digital Luxmeter (LX-1010B). The lamp was placed at a fixed distance of 20 cm from the reaction vessel. The two solutions containing 5 mL of the solution prepared by mixing 2 mg of samples, 10 ppm of MB in neutral pH and distilled water, were stirred at ambient temperature. To investigate the effect of H₂O₂, 1 mL of H₂O₂ was added to the solutions and the reactions were continued under these conditions. The photocatalytic degradation of MB under the visible light irradiation over 2 mg samples in the absence and presence of 1 mL of H₂O₂ is shown in Fig. S5a, b and Fig. 8a, b. Upon increasing the irradiation time, the absorbance of the residual dye decreases to total photodegradation after 7 and 4 min for sample 1 and 40 and 10 min for sample 2 in the absence and presence of 1 mL of H₂O₂, respectively. The photocatalytic degradation of MB

under the visible light irradiation after 80 min for TiO₂ P-25 (2 mg) is shown in Fig. S5c. Hydrogen peroxide (H₂O₂) was used as the electron acceptor to prevent the recombination of e⁻/h⁺ pairs, which reduces the photocatalytic efficiency. According to the results, sample 1 has a higher photocatalytic activity than sample 2 because of its smaller band gap, which facilitates the electron transfer to the conductive band of TiO₂ [53–55].

Generally, photogenerated holes (h⁺), hydroxyl radicals (·OH), and superoxide radicals (·O₂⁻) are the active species applied in the photocatalytic degradation of dyes. EDTA, BQ, and IPA scavengers were used to study the effects of h⁺, ·O₂⁻, and ·OH, respectively. Photodegradation efficiency (%) of MB using different scavengers for two samples is shown in Fig. 9. As observed, MB is degraded by 85%, 67%, and 34% in BQ, IPA, and EDTA, respectively. It is found that the hydroxyl radical (·OH) is the main active species in the degradation process of MB for sample 1. Moreover, MB is degraded by 76%, 90%, and 46% in EDTA, BQ, and IPA, respectively. The results show that the hole (h⁺) is the main active species in the degradation process of MB for sample 2 [56].

3.3.1 Kinetic investigation

The plots of $-\ln(A/A_0)$ of M.B vs. irradiation time (in which A₀ and A are the absorbance values at t = 0 and

Fig. 8 Photocatalytic degradation of MB under the visible light irradiation in the presence of 1 ml of H₂O₂ **a** sample 1; **b** sample 2

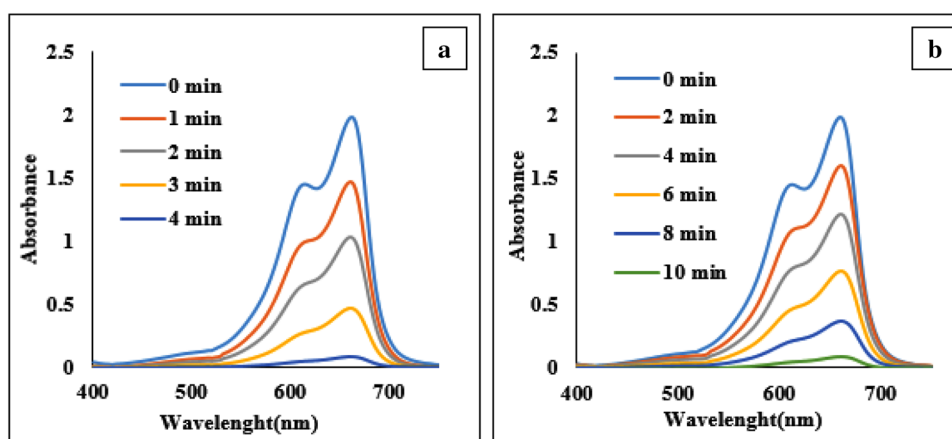


Fig. 9 Degradation efficiency (%) of MB in the presence of different scavengers **a** sample 1; **b** sample 2

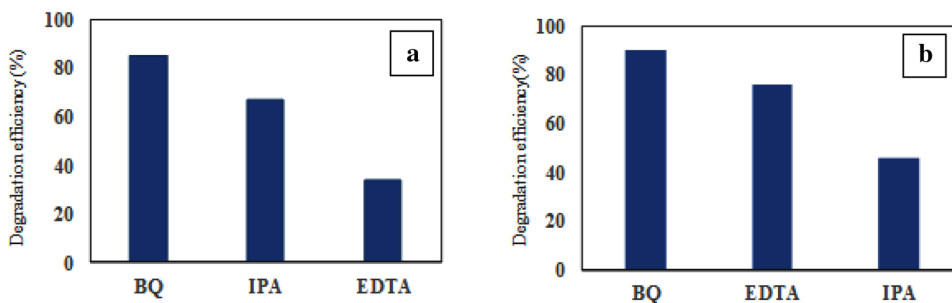


Fig. 10 Recovery of **a** sample 1; **b** sample 2 in the degradation reaction of MB in the presence of H_2O_2

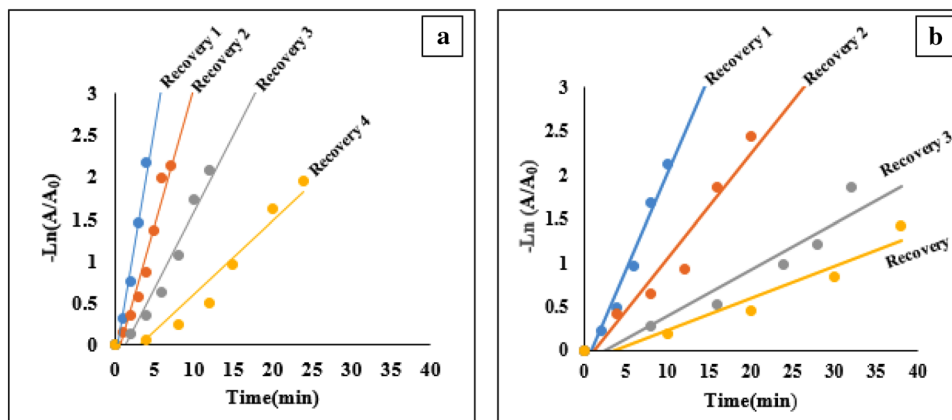


Table 3 Recovery of sample 1 in the degradation reaction of MB in the presence of H_2O_2

Number of recovery	1	2	3	4
Time (min)	4	7	12	24
Rate constant	0.548	0.327	0.181	0.088

Table 4 Recovery of sample 2 in the degradation reaction of MB in the presence of H_2O_2

Number of recovery	1	2	3	4
Time (min)	10	20	32	40
Rate constant	0.222	0.120	0.053	0.043

Table 5 Degradation of MB with other catalysts

Catalyst	Concentration (ppm)	Amount of catalyst	Time of photodegradation (min)	Source of light	References
TiO_2/Fe_2O_3	20	5 mg	120	Visible	[47]
V– TiO_2	10	0.2 g	60	Visible	[57]
Co– TiO_2	10	0.2 g	60	Visible	[57]
TiO_2 nanoparticles	10	25 mg	150	UV–Visible	[58]
CuO–CoO/ TiO_2 in presence of H_2O_2	10	2 mg	4	Visible	This study
CuO–CoO/ TiO_2 without H_2O_2	10	2 mg	7	Visible	

time (t), respectively) for samples 1 and 2 in the absence and presence of 1 mL of H_2O_2 are shown in Fig. S6. All the plots are linear. Thus, the photocatalytic degradation of MB follows pseudo first-order kinetics. Therefore, it is reasonable to assess the slopes of the plots of $-\ln(A/A_0)$ of M.B vs. irradiation time as the observed rate constants (k_{obs}) of photocatalytic degradation process. The recyclability of samples 1 and 2 was then studied in the degradation experiments under simulated visible light irradiation. The degradation time of MB in the presence

of 1 mL of H_2O_2 increased to 24 and 40 min for samples 1 and 2, respectively, over 4 cycles (Fig. 10a, b). This increase in degradation time may be attributed to the reduction of TiO_2 active sites during the photodegradation reactions. Tables 3 and 4 summarize all the rate constants evaluated.

Some reported photocatalytic degradation of MB were collected on Table 5 [47, 57, 58]. Based on these results, the best time for degradation of MB through visible light is 60 min for 10 ppm of dye via 0.2 g of catalyst [57]. In this study, in presence of 2 mg of photocatalyst, in addition to use of visible light as source of energy the time of degradation were reduced to 4 and 7 min for CuO–CoO/ TiO_2 nanotube/nanosheet in the presence of H_2O_2 and without H_2O_2 , respectively.

3.4 Catalytic reduction of P-nitrophenol using $NaBH_4$ and samples 1 and 2

The catalytic activity of both samples was evaluated in the reduction of PNP to PAP. An aqueous solution of 1.5 mL of 1×10^{-4} mM P-nitrophenol and 0.5 mL of fresh 1×10^{-2} mM $NaBH_4$ were poured into a quartz cell. The solutions containing 2 mg of the sample were then added to the mixture to initiate the reduction reaction. UV–Vis spectroscopy

Fig. 11 Catalytic reaction of PNP in the presence of NaBH_4 a sample 1; b sample 2

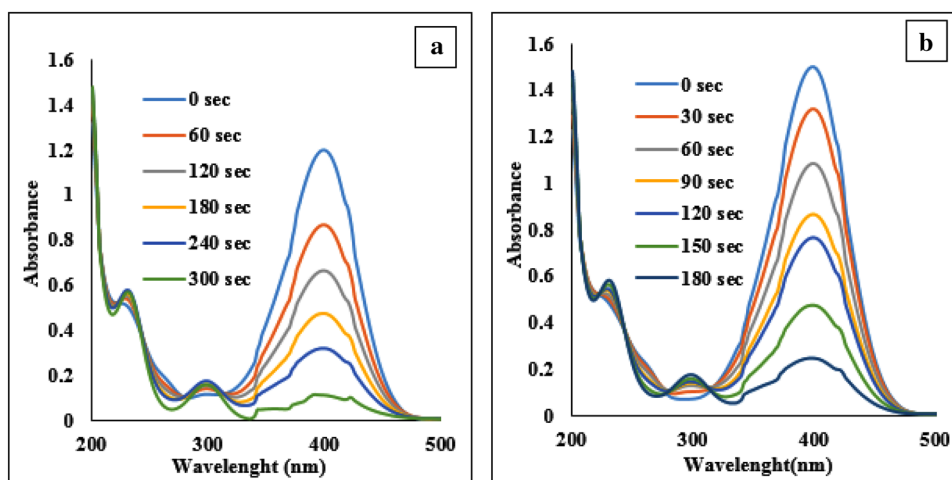
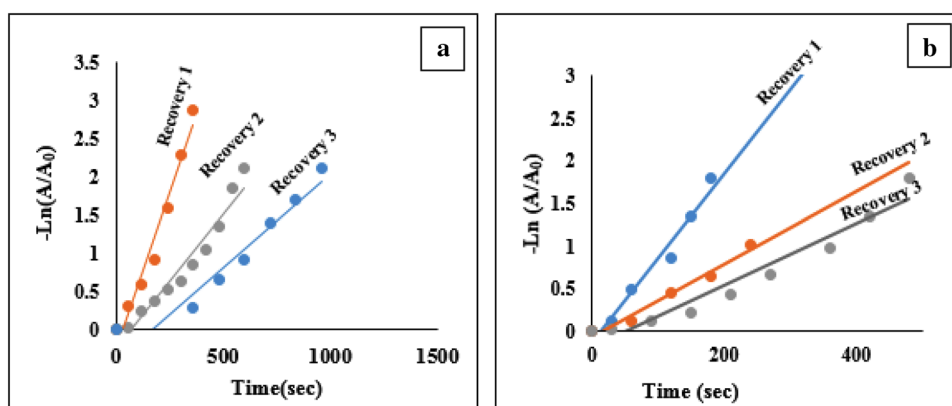


Fig. 12 Recovery of a sample 1; b sample 2 in the reduction of PNP in the presence of NaBH_4



was used to follow the progress of the reaction. The original adsorption peak of 4-nitrophenol observed at 317 nm, red-shifted to 400 nm and the color of the mixture changed from yellow to bright yellow upon the addition of NaBH_4 due to the formation of PNP ions. PNP reduction was very slow in the presence of NaBH_4 without the catalyst. The reduction of PNP was observed to complete in 5 and 3 min for samples 1 and 2, respectively. The 400 nm peak sharply decreased and a typical absorption peak at 300 nm significantly increased due to the formation of PAP (Fig. 11). The slopes of the plots of $-\ln(A/A_0)$ for PNP vs. time at 400 nm as the observed rate constants (k_{obs}) of catalytic process were assessed by the good linear correlation (Fig. S7). Sample 2 has a better catalytic activity than sample 1, according to the results since the surface area of sample 2 was higher.

The recyclability of the two samples in the reduction of 1×10^{-4} mM 4-nitrophenol to 4-aminophenol in aqueous 1×10^{-2} mM NaBH_4 was evaluated. The time reduction extent increased to 14 and 8 min for samples 1 and 2, respectively, over 3 cycles (Fig. 12). Tables 6 and 7 summarize all the rate constants evaluated.

Table 6 Recovery of sample 1 in the reduction of PNP

Number of recovery	1	2	3
Time (min)	6	10	14
Rate constant	0.008	0.003	0.002

Table 7 Recovery of sample 2 in the reduction of PNP

Number of recovery	1	2	3
Time (s)	180	240	480
Rate constant	0.009	0.004	0.003

3.5 ICP

To prepare the samples for ICP analysis, a certain amount of sample 1 or 2 was dissolved in 15 M nitric acid prior to and following the reduction of P-nitrophenol and photo-degradation of MB. This analysis was used to evaluate Cu

Table 8 ICP analysis of sample 1

Reaction	Cu (ppm)	Co (ppm)
Before reduction of PNP and photo-degradation of MB	19.43	18.87
After reduction of PNP	18.68	17.96
After photodegradation of MB	18.29	17.12

Table 9 ICP analysis of sample 2

Reaction	Cu (ppm)	Co (ppm)
Before reduction of PNP and photo-degradation of MB	24.53	21.09
After reduction of PNP	23.76	20.69
After photodegradation of MB	22.85	20.43

and Co weights. A solution, which contained 10 ppm of the sample, was prepared for this purpose. The results are as follows in Tables 8 and 9.

4 Conclusion

Two samples have been successfully prepared by hydrothermal method using Co/Cu nitrate (sample 1) and Co/Cu acetylacetonate (sample 2). According to the results, the surface properties and catalytic and photocatalytic activities were affected by the type of the metal salt. Samples 1 and 2 had nanotube/nanosheets and nanoparticle morphologies, respectively. Cu and Co were incorporated on TiO₂ as CuO and CoO, respectively. The CuO–CoO/TiO₂ nanotubes/nanosheets (sample 1) with lower band gap degraded MB in 4 min in the presence of H₂O₂ using a Tungsten Lamp. In addition, the catalytic reduction of 4-nitrophenol by NaBH₄ was carried out using each of the samples. Sample 2 with greater surface area was a better catalyst in the reduction of PNP.

Acknowledgements This research was supported by Isfahan University of Technology. We are grateful to our colleagues from Isfahan University of Technology who provided insight and expertise.

Compliance with ethical standards

Conflict of interest The authors declare that they have no known competing financial interests or personal relationships that could have appeared to influence the work reported in this paper.

References

1. M. Montazerzohori, M. Nasr-Esfahani, Z. Moradi-Shammi, A. Malekhoseini, J. Ind. Eng. Chem. (2015). <https://doi.org/10.1016/j.jiec.2014.05.014>
2. H. Safardoust-Hojaghan, M. Salavati-Niasari, J. Clean. Prod. (2017). <https://doi.org/10.1016/j.jclepro.2017.01.169>
3. M.H. Razali, A.F. Noor, M. Yusoff, Int. Res. J. Eng. Technol. **2**, 92 (2015)
4. M.N. Subramaniam, P.S. Goh, N. Abdullah, W.J. Lau, B.C. Ng, A.F. Ismail, J. Nanopart. Res. (2017). <https://doi.org/10.1007/s11051-017-3920-9>
5. K. Karami, N.S. Mousavi, Dalton Trans. (2018). <https://doi.org/10.1039/C7DT04669C>
6. E.I. Abd, I.H. Maksod, T.S. Saleh, Green Chem. Lett. Rev. (2010). <https://doi.org/10.1080/17518251003596143>
7. T.R. Mandlimath, B. Gopal, J. Mol. Catal. A (2011). <https://doi.org/10.1016/j.molcata.2011.08.009>
8. K. Sravanthi, D. Ayodhya, P.Y. Swamy, Mater. Sci. Eng. Technol. (2019). <https://doi.org/10.1016/j.mset.2019.02.003>
9. J. Jalali, M. Mozammell, M. OjaghiIlkhchi, J. Mater. Sci. Mater. Electron. (2017). <https://doi.org/10.1007/s10854-017-7592-0>
10. S. Islam, S.K. Bormon, M. Nadim, K. Hossain, A. Habib, T.S. Islam, Am. J. Anal. Chem. (2014). <https://doi.org/10.4236/ajac.2014.58057>
11. E. Forgacs, T. Cserhati, G. Oros, Environ. Int. (2004). <https://doi.org/10.1016/j.envint.2004.02.001>
12. M.T. Yagub, T.K. Sen, S. Afroze, H.M. Ang, Adv. Colloid Interface Sci. (2014). <https://doi.org/10.1016/j.cis.2014.04.002>
13. A. Vosoughifar, J. Mater. Sci. Mater. Electron. (2017). <https://doi.org/10.1007/s10854-017-8254-y>
14. W. Ouyang, F. Teng, X. Fang, Adv. Funct. Mater. (2018). <https://doi.org/10.1002/adfm.201707178>
15. W. Hong-Yu, K.E. Yang, S.I. Yuan, H. Wei-Qing, H.U. Wangyu, G.F. Huang, RRL (2018). <https://doi.org/10.1002/pssr.201800565>
16. S. Han, L. Hu, N. Gao, A. Ghamdi, X. Fang, Adv. Energy Mater. (2020). <https://doi.org/10.1002/adfm.201400012>
17. L. Zheng, F. Teng, X. Ye, H. Zheng, X. Fang, Adv. Funct. Mater. (2020). <https://doi.org/10.1002/aenm.201902355>
18. S. Bae, S. Gim, H. Kim, K. Hanna, Appl. Catal. B (2016). <https://doi.org/10.1016/j.apcatb.2015.10.006>
19. A. Gołębiewska, W. Lisowski, M. Jarek, G. Nowaczyk, A. Zielińska-Jurek, Appl. Surf. Sci. (2014). <https://doi.org/10.1016/j.apsusc.2014.09.039>
20. N. Singhal, U. Kumar, Mol. Cat. (2017). <https://doi.org/10.1016/j.mcat.2017.06.031>
21. B.X. Zhou, S.S. Ding, Y. Wang, X.R. Wang, W.Q. Huang, K. Li, G.F. Huang, Nanoscale (2020). <https://doi.org/10.1039/D0NR0176G>
22. Y.Y. Li, Y. Si, B.X. Zhou, W.Q. Huang, W. Hu, A. Pan, X. Fan, G.F. Huang, Nanoscale (2019). <https://doi.org/10.1039/C9NR05413H>
23. Q. Yuan, X. Guan, X. Xue, D. Han, H. Zhong, W. Ji, RRL (2019). <https://doi.org/10.1002/pssr.201800575>
24. A.G. Escobar-Villanueva, V.M. Ovando-Medina, H. Martinez-Gutierrez, M.P. Militello, J. Mater. Sci. Mater. Electron. (2020). <https://doi.org/10.1007/s10854-019-02644-8>
25. A. Pérez-Larios, R. Gomez, Avances: Investigación en Ingeniería (2013). <https://doi.org/10.1016/j.cattod.2011.02.011.7.M>
26. D. Guerrero-Araque, P. Acevedo-Peña, D. Ramírez-Ortega, L. Lartundo-Rojas, R. Gómez, J. Chem. Technol. Biotechnol. (2017). <https://doi.org/10.1002/jctb.5273>
27. Y. Wang, Y. He, Q. Lai, M. Fan, J. Environ. Science (2014). <https://doi.org/10.1016/j.jes.2014.09.023>

28. A.H. Kianfar, M.A. Arayesh, J. Environ. Chem. Eng. (2020). <https://doi.org/10.1016/j.jece.2019.103640>
29. A.H. Kianfar, P. Dehghani, M.M. Momeni, J. Mater. Sci. Mater. Electron. (2016). <https://doi.org/10.1007/s10854-015-4167-9>
30. M. Dostani, A.H. Kianfar, M.M. Momeni, J. Mater. Sci. Mater. Electron. (2017). <https://doi.org/10.1007/s10854-016-5568-0>
31. T.H. Vu, H.T. Au, L.T. Tran, T.M. Nguyen, T.T. Tran, M.T. Pham, M.H. Do, D.L. Nguyen, J. Mater. Sci. Mater. Electron. (2014). <https://doi.org/10.1007/s10853-014-8274-4>
32. H. Tian, S.Z. Kang, X. Li, L. Qin, L.M. Ji, J. Mu, Sol. Energy Mater. Sol. Cells. (2015). <https://doi.org/10.1016/j.solmat.2014.12.016>
33. N.M. Mohamed, R. Bashiri, F.K. Chong, S. Sufian, S. Kakooei, Int. J. Hydrogen Energy (2015). <https://doi.org/10.1016/j.ijhydene.2015.07.064>
34. G. Dai, L. Zhao, S. Wang, J. Hu, B. Dong, H. Lu, J. Li, J. Alloys Compd. (2012). <https://doi.org/10.1016/j.jallcom.2012.06.046>
35. X. Cheng, X. Gui, Z. Lin, Y. Zheng, M. Liu, R. Zhan, Y. Zhu, Z. Tang, J. Mater. Chem. (2015). <https://doi.org/10.1039/C5TA03635F>
36. X. Xu, L. Hu, N. Gao, S. Liu, S. Wageh, A.A. Al-Ghamdi, A. Alshahrie, X. Fang, Adv. Funct. Mater. (2016). <https://doi.org/10.1002/adfm.201403065>
37. R. Camposeco, S. Castillo, J. Navarrete, R. Gomez, Catal Today (2016). <https://doi.org/10.1016/j.cattod.2015.09.018>
38. L. Zheng, S. Han, H. Liu, P. Yu, X. Fang, Small (2016). <https://doi.org/10.1002/sml.201503441>
39. Y. Wang, W. Duan, B. Liu, X. Chen, F. Yang, J. Nanomater. (2014). <https://doi.org/10.1155/2014/178152>
40. M.H. Barakat, G. Hayes, S.I. Shah, J. Nanosci. Nanotechnol. (2005). <https://doi.org/10.1166/jnn.2005.087>
41. S. Mathew, P. Ganguly, S. Rhatigan, V. Kumaravel, C. Byrne, S. Hinder, J. Bartlett, M. Nolan, S.C. Pillai, Appl. Sci. **9**, 12 (2018)
42. N.L. Reddy, S. Kumar, V. Krishnan, M. Sathish, M.V. Shankar, J. Catal. (2017). <https://doi.org/10.1016/j.jcat.2017.02.032>
43. T.H. Nguyen, T.L. Nguyen, T.D. Ung, Q.L. Nguyen, Adv. Nat. Sci. Nanosci. Nanotechnol. (2013). <https://doi.org/10.1088/2043-6262/4/2/025002>
44. G. Westin, K. Jansson, A. Pohl, M. Leideborg, J. Sol-Gel. Sci. Technol (2004). <https://doi.org/10.1023/B:JSST.0000047955.86479>
45. M.H. Razali, A.F. Mohd-Noor, A.R. Mohamed, S. Sreekantan, J. Nanomater. (2012). <https://doi.org/10.1155/2012/962073>
46. D. Lu, O.A. Zelekew, A.K. Abay, Q. Huang, X. Chen, Y. Zheng, RSC Adv. (2019). <https://doi.org/10.1039/C8RA09645G>
47. L. Cheng, S. Qiu, J. Chen, J. Shao, S. Cao, Mater. Chem. Phys. (2017). <https://doi.org/10.1016/j.matchemphys.2017.01.001>
48. Y.Y. Li, Y. Si, B.X. Zhou, T. Huang, W.Q. Huang, W. Hu, A. Pan, X. Fan, G.F. Huang, Nanoscale (2020). <https://doi.org/10.1039/C9NR09945J>
49. I. Kustiningsih, W.W. Purwanto, J. Technol. **5**, 133 (2014)
50. A. Gołębiewska, W. Lisowski, M. Jarek, G. Nowaczyk, M. Michalska, S. Jurga, A. Zaleska-Medynska, Mol. Catal. (2017). <https://doi.org/10.1016/j.mcat.2017.09.004>
51. A. Monga, R.A. Rather, B. Pal, Sol. Energy Mater. Sol. Cells (2017). <https://doi.org/10.1016/j.solmat.2017.08.002>
52. A. Bayat, E. Saievar-Iranizad, J. Alloys Compd. (2018). <https://doi.org/10.1016/j.jallcom.2018.05.008>
53. M.H. Habibi, R. Kamrani, Desalin Water Treat. (2012). <https://doi.org/10.1080/19443994.2012.677512>
54. S. Liu, L. Zheng, P. Yu, S. Han, X. Fang, Adv. Funct. Mater. (2014). <https://doi.org/10.1002/adfm.201505554>
55. S. Han, L. Hu, Z. Liang, S. Wageh, A.A. Al-Ghamdi, Y. Chen, X. Fang, Adv. Funct. Mater. (2014). <https://doi.org/10.1002/adfm.201401279>
56. J. Zhang, Q. Liu, H. He, F. Shi, G. Huang, B. Xing, J. Jia, C. Zhang, Carbon (2019). <https://doi.org/10.1016/j.carbon.2019.06.034>
57. T. Lv, J. Zhao, M. Chen, K. Shen, D. Zhang, J. Zhang, G. Zhang, Q. Liu, Materials (2018). <https://doi.org/10.3390/ma11101946>
58. C. Hou, B. Hu, J. Zhu, Catalysts (2018). <https://doi.org/10.3390/catal8120575>

Publisher's Note Springer Nature remains neutral with regard to jurisdictional claims in published maps and institutional affiliations.